Title
Centrifuge Modeling of End-Restraint Effects in Energy Foundations

Journal
JOURNAL OF GEOTECHNICAL AND GEOENVIRONMENTAL ENGINEERING, 141(8)

ISSN
1090-0241

Authors
Goode, JCIII
McCartney, John S

Publication Date
2015

DOI
10.1061/(ASCE)GT.1943-5606.0001333

Peer reviewed

CENTRIFUGE MODELING OF END-RESTRAINT EFFECTS IN ENERGY FOUNDATIONS

By J.C. Goode III, M.S., S.M.ASCE[1] and John S. McCartney, Ph.D., P.E., M.ASCE[2]

Abstract: This study presents the results from physical modeling experiments on centrifuge-scale energy foundations in dry sand and unsaturated silt layers. These experiments were performed to characterize end restraint effects on soil-structure interaction for energy foundations in different soils, and include tests on foundations with semi-floating and end-bearing toe boundary conditions and free- and restrained-expansion head boundary conditions. Two scale-model energy foundations having different lengths were constructed from reinforced concrete to simulate end-bearing and semi-floating conditions in soil layers having the same thickness. The foundations include embedded thermocouples and strain gages, which were calibrated under applied mechanical loads and nonisothermal conditions before testing. The variables measured during the experiments include axial strain and temperature distributions in the foundation, temperature and volumetric water content measurements in the soil, vertical displacements of the foundation head and soil surface, and axial stress at the foundation head. These variables were used to calculate the distributions in thermal axial stress and thermal axial displacement, which are useful in evaluating soil-structure interaction mechanisms. The results confirm observations from full-scale energy foundations in the field for end-bearing foundations, and provide new insight into the behavior of semi-floating foundations. Heating of the semi-floating foundations in compacted silt led to a clear increase in ultimate capacity, potentially due to changes in radial normal stress and thermally-induced water flow, while heating of the semi-floating foundations in dry sand led to a negligible change in ultimate capacity.

[1] Engineer, Shannon and Wilson, Denver, CO
[2] Associate Professor, Department of Structural Engineering, University of California San Diego, 9500 Gilman Dr. La Jolla, CA 92093-0085

INTRODUCTION

The effects of incorporating geothermal heat exchangers into subsurface infrastructure is an emerging topic in geotechnical engineering. In particular, the incorporation of heat exchangers into drilled shaft foundations has been shown to provide a sustainable approach to transfer thermal energy to and from the ground for a lower installation cost than traditional borehole-type geothermal heat exchangers (Brandl 1998; Brandl 2006). Observations from several case histories involving full-scale energy foundations indicate that heating and cooling will lead to movements associated with thermal expansion and contraction of the foundation element and surrounding soil (Laloui et al. 2003; Brandl 2006; Laloui et al. 2006; Bourne-Webb et al. 2009; Bouazza et al. 2011; Amatya et al. 2012; McCartney and Murphy 2012; Akrouch et al. 2014; Murphy et al. 2014; Sutman et al. 2014; Murphy and McCartney 2014; Wang et al. 2014a). These thermally-induced movements may lead to the generation of axial stresses due to the restraint of the foundation provided by soil-structure interaction and end-restraint boundary conditions. Although the role of end-restraint boundary conditions at the head and toe of the foundation has been assessed qualitatively in some of these studies (Laloui et al. 2006; Amatya et al. 2012; Murphy et al. 2014), it has not been evaluated thoroughly due to the complexity associated with understanding these conditions in a full-scale site. The end-restraint boundary conditions may play an important role in design guidelines which are being proposed for energy foundations (Suryatriyastuti et al. 2013; Mimouni and Laloui 2014).

This study involves the use of physical modeling tests in a geotechnical centrifuge to evaluate the effects of end-restraint boundary conditions on energy foundations following an approach introduced by Stewart and McCartney (2014). Stewart and McCartney (2014) evaluated transient heating and cooling of a centrifuge-scale energy foundation with end-bearing boundary conditions, and showed using a single test how instrumentation could be used to assess soil-structure interaction mechanisms. The results from their centrifuge tests and those from following studies (Goode et al. 2014, Goode and McCartney 2014) have been compared with numerical simulations (Wang et al. 2012, 2014b), with heat transfer being considered in model scale. Although centrifuge tests represent a comparatively simple situation compared to field tests, they still provide empirical data that can be used for calibration of parameters or verification of load transfer analyses (Knellwolf et al. 2011) and finite element analyses (Laloui et al. 2006; Wang et al. 2012, 2014b; Ouayang et al. 2012).

An advantage of physical modeling in the centrifuge over full-scale testing is that the properties of scale-model foundations and soil layers can be carefully controlled and different configurations can be considered for lower costs. Centrifuge modeling also permits incorporation of dense instrumentation arrays to capture thermo-mechanical effects in the energy foundation as well as thermo-hydro-mechanical effects in the surrounding soil, both of which are necessary to validate predictions from finite element analyses. Another advantage of centrifuge modeling is that scale-model energy foundations can be loaded to failure to destructively characterize the effects of temperature on the load-settlement curve and the associated ultimate side shear resistance and end bearing (McCartney and Rosenberg 2011).

The objective of this study is to present the results from a series of centrifuge modeling experiments to quantify the role of end restraint boundary conditions at the foundation head and toe in dry sand and unsaturated silt. The approach described by Stewart and McCartney (2013) to consider the centrifuge scaling conflict between geometric similitude and heat flow is used in this study. Specifically, the tests in this study were performed by bringing a scale-model energy foundation to a target temperature, then performing different loading tests. In this case, the results are expected to represent a worst-case scenario, as heat flow in the centrifuge model will have affected a greater zone of soil than that affected by a prototype foundation in the field heated for the same scaled time. Nonetheless, the relatively stiff silt and dry sand evaluated in this study will not be as significantly affected by temperature changes as soft clays would, so this worst-case scenario is not expected to differ significantly from a heating test on a full-scale energy foundation in these soil profiles. A discussion on the calculation of thermal axial stresses and thermal axial displacements from measured values of thermal axial strain is presented in Stewart and McCartney (2014) and Murphy et al. (2014), so these calculations are not presented again in this paper for the sake of brevity. This paper uses the same sign conventions as these previous studies, where positive values of thermal axial strain and stress denote compression, and positive displacements denote downward movement.

BACKGROUND

Several field studies have evaluated the distributions in thermal axial strain and stress in full-scale energy foundations. Laloui et al. (2003, 2006) observed increases in thermal axial stress with depth during heating tests on a 25 m-long energy foundation installed in an overconsolidated soil deposit after different stories of a building were constructed. The head of the foundation in a test performed before building construction heaved upward by 4.2 mm (i.e., -4.2mm displacement) during heating to 21 °C. Bourne-Webb et al. (2009) and Amatya et al. (2012) also observed an increase in compressive forces during heating of a 23 m-long energy foundation installed in a layered clay deposit loaded axially from the surface using a load frame. They used fiber optic sensors to measure a continuous distribution in thermal axial strain with depth, and observed tensile thermal axial stresses at the toe of the foundation during cooling. Bouazza et al. (2011) and Wang et al. (2014a) used a pair of Osterberg cells embedded in an energy foundation to translate a section of the shaft upward and downward to characterize changes in side shear resistance with temperature. McCartney and Murphy (2012) and Murphy and McCartney (2014) evaluated the stresses and strains in a pair of 12.7 m-long energy foundations beneath an 8-story building during typical heat pump operations, and observed both the greatest compressive and tensile thermal axial stresses near the toe of the foundation during heating and cooling, respectively. Murphy et al. (2014) characterized soil structure interaction mechanisms including distributions in thermal axial stress, strain, displacement and mobilized side shear for three end-bearing foundations in a sandstone deposit. They observed that differences in head restraint provided by the overlying building had an effect on the magnitude of thermally-induced stresses and displacements.

Bourne-Webb et al. (2009) proposed hypothetical representations of the mechanisms of thermo-mechanical soil-structure interaction in “floating” energy foundations that have no end bearing, and Amatya et al. (2012) extended these representations to cases with non-zero end-bearing (semi-floating and end-bearing conditions). A floating foundation is expected to expand about its center during uniform heating, an end-bearing foundation is expected to expand upward from the base, and a semi-floating foundation is expected to have an intermediate response. Knellwolf et al. (2011) referred to the point of zero thermal axial displacement about which the foundation expands during heating as the null point, and noted that this is an important parameter in thermo-mechanical soil-structure interaction analyses. The null point is typically near the toe of the foundation for end-bearing energy foundations (Stewart and McCartney 2013; Murphy et al. 2014). Although the location of the null point for semi-floating foundations is expected to be near the center of the foundation, the behavior of these foundations in the field hasn’t been well characterized. The hypothetical representations of soil-structure interaction mechanisms of

Bourne-Webb et al. (2009) and Amatya et al. (2012) are useful when evaluating field measurements and simulation results, especially when differentiating the effects of temperature from those of mechanical loading on the distributions in axial stress and side shear resistance.

MATERIALS

Nevada Sand

Six of the tests in this study were performed on energy foundations in a layer of dry Nevada sand having a relative density of 60% (void ratio of 0.75). The sand consists of uniform angular particles, and based on the characteristic grain size values shown in Table 1 has a Unified Soil Classification System (USCS) classification of SP (poorly graded sand). At a relative density of 60% and a mean stress of 100 kPa, Nevada sand has a friction angle of 35°, a shear modulus of 30 MPa, and a Poisson's ratio of 0.3. The thermal conductivity measured using a KD2Pro thermal needle from Decagon Devices of Pullman, WA was 0.265 W/mK. The sand layers were prepared using air pluviation around the energy foundation.

Bonny Silt

Four of the tests in this study were performed on energy foundations installed in a layer of Bonny silt, which is the same soil used by Stewart and McCartney (2013). Relevant geotechnical properties of Bonny silt are also summarized in Table 1. The liquid and plastic limits are 26 and 24 and the fines content is 84%, so Bonny silt has a USCS classification of ML (inorganic silt). The silt has a specific gravity G_s of 2.6. The silt layer was prepared using compaction to permit fast model preparation times and to reach uniform distributions in dry unit weight and water content with height at the beginning of the tests. The soil layers were prepared by compacting silt having a gravimetric water content of 14.2% in 76.2 mm-thick lifts around the foundation to reach a target dry density of 1565 kg/m^3. A rubber mallet was used to compact the soil around the foundation in 75 mm-thick lifts. The centrifuge test was performed on the soil layer in as-compacted (unsaturated) conditions. The thermal conductivity of the silt under these compaction conditions was 1.20 W/mK.

Scale-Model Energy Foundations

Two scale-model energy foundation having a diameter of 63.5 mm were fabricated for this study. One of the foundations has a length of 342.9 mm (short foundation), while the other has a length of 533.4 mm (long foundation). A centrifuge acceleration of 24g was used in all of the tests, so the corresponding prototype-scale short and long foundations have a diameter of 1.5 m and lengths of 8.2 m and 12.7 m, respectively. The foundation diameter is greater than that of Stewart and McCartney (2014) to provide more space around embedded instrumentation. Schematics of the foundations are shown in Figure 1.

Although drilled shafts are typically cast-in-place, the model foundations were precast in a cardboard mold having an inside diameter of 63.5 mm to ensure quality construction considering the extensive embedded instrumentation. The reinforcing cage was formed from welded steel hardware cloth that simulates the longitudinal and lateral members of a drilled shaft reinforcing cage. The cage has 12.7 mm-square openings, with 19 gage wire thickness. The cage diameter is 48.5 mm, leaving a concrete cover of 7.5 mm on the sides and 6.35 mm on the top and bottom. The cage openings were larger than those of Stewart and McCartney (2014), permitting use of a concrete mixture consisting of 1:2:1.5:1.5 water:cement:sand:coarse aggregate ratio. This mixture has a larger coarse aggregate fraction and greater size of coarse aggregates (7 mm max) than that of Stewart and McCartney (2014), making it closer to the mixture used in drilled shafts.

Seven strain gages and thermocouples were embedded within the foundation to characterize the strain response and temperature distribution within the foundations. The strain gages were model CEA-13-250UW-350 from Vishay Precision Group, and were bonded using M-Bond AE-15 epoxy to 50.8 mm-long, 12.7 mm-wide, and 1.8 mm-thick steel tabs. The tabs have two 6.1 mm-diameter holes at top and bottom for good interaction with the concrete, and the zinc plating on the tabs was sanded off to provide a smooth surface. The bonded gages were cured under pressure for 4 hours at 57.2 °C. A Teflon strip was placed over the cured gage, which was then covered using a waterproof epoxy (Gagekote #5). Miniature thermocouples (Fine wire type K Model STC TT K 36 3C from Omega) were attached to the steel tabs next to the strain gages. The finished steel tabs were attached to the inside of the reinforcing cage using thin wire thread at the locations in Figure 1. The gages were installed on opposing sides of the reinforcing cage on an alternating basis because of space constraints with the wiring. In addition to the embedded instrumentation, three heat exchanger loops were affixed to the inside of the reinforcing cage at an equal spaced around the circumference of the cage. Perfluoroalkoxy (PFA) tubing with an inside diameter of 3.175 mm was used for the heat exchange loops. The bottom of the loops were tied to the cage so that they do not cross through the center of the foundation.

After the cage and instrumentation were centered in the form, concrete was placed using a miniature tremie pipe to ensure uniform concrete placement. The form was placed on a vibrating table during concrete placement for good concrete flow and for extruding entrapped air. When the concrete had reached the top of the form, a hex-head bolt was placed in the middle of the foundation to provide a centering point for mechanical loading of the foundation. The foundations were cured in a fog room for 14 days, after which 14 more days of curing were permitted after removing the form.

Before construction of the foundations, thermo-mechanical calibration tests were performed on the assembled strain gages by hanging a 27 kg mass from the steel tabs, then heating them with a hot air gun (fixed at a distance of 300 mm from the gage to avoid overheating). The results of one of the calibration tests on a gage-tab assembly are shown in Figure 2(a). After reversing the sign of the gage reading so that compression is defined as positive, the raw gage readings showed negative strains during application of the tensile force, as expected. However, heating was observed to lead to a reversal of the trend in strain due to differential thermal expansion of the gauge, steel tab, and epoxy. To account for this behavior, a thermo-mechanical correction was applied so that the measurements from the gages would yield strains that are consistent with the properties of steel (i.e., a Young's modulus of E_{steel} = 200 GPa and a coefficient of linear thermal expansion of α_{steel} = -13.0 $\mu\varepsilon$/°C), as follows:

$$\varepsilon_{tab} = \chi\varepsilon_{raw} + \Delta T\beta \quad (1)$$

where χ and β are mechanical and thermal correction factors, respectively, which were defined individually for each gage. The values of χ ranged from 0.34 to 0.52 and the values of β ranged from -24.9 to -28.4 (Goode 2013). Although these correction factors differed slightly due to variability in the assembly of the gages, the same pattern of behavior was observed in each gage. Repeat tests on each gage revealed the same correction factors.

After curing, tests were performed on the foundations to characterize their thermo-mechanical response. First, the foundation was loaded mechanically in stages in a load frame to evaluate the Young's modulus of the reinforced concrete, then was heated under free-expansion conditions to evaluate the coefficient of linear thermal expansion. In these tests, it was observed that the strains calculated using Equation (1) differed from the global foundation strain inferred from the head displacement measured using a linearly variable differential transformer (LVDT), potentially due to embedment and alignment effects in the reinforced concrete. Accordingly, a second calibration equation was defined for each gage, as follows:

$$\varepsilon = \mu\varepsilon_{tab} + \Delta T \xi \qquad (2)$$

where ε is the thermo-mechanical strain, μ is a mechanical correction factor for embedment effects, and ξ is a thermal correction factor for embedment effects.

An example of the corrected strain values during mechanical loading of the long foundation in even increments of axial stress from 281 to 706 kPa is shown in Figure 2(b). Although the effects of bending are observed in the gages due to the unrestrained length of the relatively slender foundation, a linear trend in mechanical strains with increasing axial stress is observed. A multiplicative correction factor of $\mu = 0.5$ was used for all of the gages to to match the global strain values for the reinforced concrete calculated from the LVDT measurements, which are shown at a depth of zero in Figure 2(b). The same mechanical correction factor was used for all of the gages to avoid covering up the effects of bending observed in the strain profiles. The global strain values from the LVDT correspond to a Young's modulus of 33 GPa, which is similar to the value expected for drilled shafts (~30 GPa).

The free-expansion heating tests were performed on the foundations by circulating water having a temperature of 55 °C through the heat exchange tubing when the foundation was standing vertically on a rigid base (Goode 2013). During the free expansion tests, it was expected that all of the gages would show the same strain values for a given temperature, as the foundation was unrestrained. However, there were some slight differences with height that were attributed to varying distances from the heat exchanger tubing to the gages, differential expansion of the steel tabs and the surrounding concrete, slight variations in the alignment of the gages, and variations in the steel tab-concrete interaction (Goode 2013). Accordingly, values of ξ ranging from 3.8 to 10 were defined so that the gages show the same slope as the global thermal expansion strain defined from the LVDT displacements, as shown in Figure 2(c). The global strain inferred from the head displacements indicates that the reinforced concrete has a coefficient of thermal expansion α_c of -16 $\mu\varepsilon$/°C for the short foundation and -15 $\mu\varepsilon$/°C for the long foundation. These values are greater than those expected in drilled shafts due to the greater percentage of heat exchange tubing in the foundation cross section.

Despite the number of different corrections applied to the measured strains, all of the gages were considered in a systematic manner. The foundations were reused in several different centrifuge tests in which the gages provided consistent results. Further, after application of the corrections, the strain values from the gages consistently met several checks during the centrifuge tests, such as being equal or less than the free expansion strain of the reinforced concrete during heating. Gages 2 and 6 in the short foundation were damaged during installation, but all seven gages functioned in the long foundation.

EXPERIMENTAL SETUP

Schematics of the container used in this study to evaluate the thermo-mechanical strain distributions for the energy foundations tested in sand and silt are shown in Figure 3. The schematics show the case of the semi-floating foundation, but the same configuration was used for the end-bearing foundation with its toe resting on the bottom of the container. The container is a cylindrical aluminum tank with an inside diameter of 0.6 m, wall thickness of 13 mm, and a height of 0.54 m. A 13 mm-thick insulation sheet was wrapped around the container to minimize heat transfer through the sides of the cylinder. The bottom of the container is not insulated to provide a stiff platform for loading. The load frame consists of a steel frame mounted atop a rectangular steel platform resting on the centrifuge basket. A pneumatic piston was used to apply axial loads to the foundation in load-control conditions, and the applied load was measured using a load cell. The temperature control system developed by Stewart and McCartney (2014) was used in this study. This system is used to control the temperature of the foundation, rather than to simulate the heat exchange processes encountered in an energy foundation in the field.

The locations of instrumentation incorporated into the centrifuge container are also shown in Figure 3. Two LVDTs were placed on top of the foundation for redundancy and two others were placed on the soil surface at different radial distances from the foundation. The LVDTs were mounted on aluminum bars connected to two support beams connected to the top of the container. The LVDT readings were corrected to account for the change in the ambient temperature of the centrifuge chamber. Goode (2013) observed that a stationary LVDT showed a phantom model-scale settlement of $0.0246\Delta T_{ambient}$ (in mm), where $\Delta T_{ambient}$ is the change in temperature of the centrifuge chamber from the beginning of the test. Four thermocouple profile probes for measuring soil temperature with depth were inserted in the soil layers at different radial locations from the foundation, and dielectric sensors (model EC-TM from Decagon Devices) for measurement of volumetric water content and temperature were installed in the Bonny silt layers. The results from these sensors are not presented here but are reported by Goode (2013).

EXPERIMENTAL PROCEDURES

The same procedures were used for all of the tests on the semi-floating foundations. Seven tests were performed on the semi-floating foundations in different soil layers, as summarized in Table 2. After assembly of the container within the load frame on the centrifuge basket, the centrifuge was spun to a target centripetal acceleration of 24g. After the LVDTs on the foundations and soil indicated the system was at equilibrium, a prototype-scale axial load of approximately 360 kN (axial stress of 197 kPa) was applied to the energy foundation. The foundations were then heated to the target temperatures listed in Table 2 in load-control conditions, which means that the top of the foundation is free to move upward due to thermal expansion (i.e., negligible head stiffness). After maintaining a constant foundation temperature for at least 30 minutes, the semi-floating foundation was loaded to approximately 2400 kN then unloaded. This magnitude of head load led to a prototype-scale head settlement that was approximately 0.013 to 0.015 times the diameter of the foundations.

Three tests were performed with the end-bearing foundation, as summarized in Table 2, each with different testing procedures. The two tests on the end-bearing foundation in sand involved an evaluation of the role of head restraint. Test 8 involved a load-control heating test under an axial load of 1200 kN while Test 9 involved a stiffness control test in which a section of threaded rod was used to preload the foundation to 1000 kN. These two tests were the only two that were performed in the same sand layer, albeit on different days to permit the system to cool after the load-control test. The initial load differed between these two tests as the preloading had to be performed before spin-up of the centrifuge, and the self-weight of the load cell applied an additional load during centrifugation. Despite the difference in axial load the role of head restraint can still be evaluated from these tests. Test 10 on the end-bearing foundation in silt involved heating of the foundation in load-control conditions in stages. After reaching a steady temperature at each stage, the foundation was loaded and unloaded. Although this is not expected to cause failure, the role of heating on the slope of the load-settlement curve can be assessed.

EXPERIMENTAL RESULTS

The results from the four tests on the semi-floating foundations in sand (Tests 1-4) are shown in Figure 4. These tests were originally presented by Goode et al. (2014). The data in these figures are presented in prototype scale, so the loads and displacement during spin-up of the centrifuge are not shown. The settlement of the foundation and soil shown in this figure were zeroed at the end-of spin-up and a period of time was permitted for equilibration under the applied centripetal acceleration. The results in the top row of this figure include the settlement of the soil surface and foundation head during equilibration and application of the seating load. In all cases the foundation and soil surface quickly reached equilibrium. The results in the second row of this figure include the temperatures at different depths of the foundation. In all four tests the foundation temperature was relatively constant with depth. The temperature control system did not permit precise control of the temperature and occasionally led to fluctuations in temperature with time, but the temperatures were within 2-3 °C of the target value. The results in the bottom row show the axial strains in the foundation. Spin-up and application of the seating load led to negligible strains in the foundation. During heating of the foundations, negative strains were measured, signifying expansion. During loading and unloading of the foundation after reaching the target temperature, a clear increase in strain was measured, denoting a compressive strain superimposed atop the thermal expansion as expected. The strains due to heating are greater than those due to mechanical loading, which reflects the importance of considering thermo-mechanical effects in energy foundations.

The results from the three tests on the semi-floating foundation in Bonny silt (Tests 5-7) are shown in Figure 5. Different from the tests on Nevada sand, the results in the top row of this figure indicate that the foundation and soil continued to settle under self-weight conditions throughout the test. However, the effects of heating and subsequent mechanical loading of the foundation can clearly be observed superimposed atop the gradual settlement. As the foundation and soil were both settling by the same amount before heating started, it is expected that the effects of dragdown were not significant. The results in the middle row of the figure also indicate the foundation temperature was within 3 °C of the target value during mechanical loading.

Similar to the tests on Nevada sand, the results in the bottom row of this figure indicate that the strains due to heating are greater than the strains due to mechanical loading despite the different soil type. Although the bottom strain gage shows an inconsistent tensile strain during mechanical loading in Tests 5 and 6, the change in strain during heating is consistent with the strains in the rest of the foundation.

The results from the two tests on the end-bearing foundation in Nevada sand (Tests 8 and 9) are shown in Figure 6. These tests were originally presented by Goode and McCartney (2014). Although the settlement results in the top row of this figure indicate that the soil appears not to have reached equilibrium before mechanical loading, the scale of displacement is much smaller than that shown in Figure 4 and it can be considered to be constant. The results in Figure 6(a) clearly show the downward settlement of the foundation head during application of the foundation load, while the results in Figure 6(b) show a negligible settlement of the foundation head after spin-up of the centrifuge. The results in Figures 6(c) and 6(d) indicate that the temperatures at different depths in the foundation were relatively similar except at the bottom. This occurred because the bottom of the container was not insulated. The results in Figure 6(e) indicate that the positive compressive strains were greatest at the top of the foundation during application of the axial load as expected, while the strains in the foundation tested under stiffness control shown in Figure 6(f) were inconsistent during spin-up and equilibration. During heating, the strains in both tests mimicked the trend in the temperature of the foundations.

The results of the end-bearing foundation tested in the silt layer (Test 10) are shown in Figure 7. Similar to the tests on the semi-floating foundation in silt, the soil surface gradually settled throughout the test as shown in Figure 7(a). The foundation showed a relatively large, irrecoverable settlement during the initial loading test at room temperature. The irrecoverable displacement on the first cycle may have been due to seating of the toe of the foundation on the bottom of the container. During heating, the foundation was observed to heave upward as expected. The amount of head movement upon each loading test is similar during the subsequent cycles. The temperatures of the foundation shown in Figure 7(b) show that the target temperature was initially overshot in each of the heating stages, but eventually stabilized at the target values. The axial strains shown in Figure 7(c) clearly show the effects of loading and heating of the foundation, with greater effects observed due to heating.

ANALYSIS OF RESULTS

Effect of Soil Type on Soil-Structure Interaction in Semi-Floating Foundations

Profiles of different variables relevant to the evaluation of soil-structure interaction mechanisms in the semi-floating foundations in sand and silt layers are shown in Figures 8 and 9, respectively. The temperature distributions in the semi-floating foundations in sand and silt are shown in Figures 8(a) and 9(b), respectively, for different average changes in temperature of the foundations. These profiles were obtained at instances in time in Tests 2-4 and 6 and 7 at which the foundation had reached a stable temperature, but before mechanical loading of the foundation. In both soil layers, the temperatures were relatively constant with depth (within ±1.5 °C of the average value).

For these same instances in time, the thermal axial strains in the foundations are shown in Figures 8(b) and 9(b) for the foundations in sand and silt, respectively. The thermal axial strains were defined by zeroing the axial strains shown in Figures 4 and 5 at the beginning of heating. The thermal axial strains at a depth of zero shown in these figures were not measured using the strain gages. Instead, they correspond to the theoretical thermal axial strain of the foundation at free expansion corresponding to the average change in temperature of the foundation

($\varepsilon_{T,free} = \alpha\Delta T_{average}$). Thermal axial strains corresponding to free-expansion conditions are expected at the foundation head in these tests as they were performed under load-control conditions with negligible head restraint. The thermal axial strains at different depths in the foundations in both soil layers are relatively close to the free expansion conditions, although the foundation in silt shows greater (less negative) strains at the middle of the foundation during both tests at elevated temperatures. The distribution in thermal axial strain is much less pronounced with depth than that measured by Stewart and McCartney (2014), possibly due to the greater coefficient of thermal expansion and the greater stiffness of the foundations in this study.

The profiles of thermal axial stress are shown in Figures 8(c) and 9(c) for the foundations in sand and silt, respectively. The thermal axial stresses are equal to the Young's modulus multiplied by the difference between the measured thermal axial strain and the thermal axial strain corresponding to free expansion. In both soils, the thermal axial stresses are greatest at the center of the foundations although the middle gage shows an inconsistent behavior at high temperatures. The thermal axial stresses at the toe of the foundation are greater than those at the head, which for no head restraint is zero. Greater thermal axial stresses were observed in the foundations in silt than the foundations in sand, potentially due to greater soil structure interaction associated with the effects of compaction.

The thermal axial displacements shown in Figures 8(d) and 9(d) for the foundations in sand and silt, respectively, were obtained by integrating the thermal axial strains with depth and subtracting these values from the head displacements measured using the LVDT (shown as the thermal axial displacement at a depth of 0). The slope of the displacement profile reflects the relative movement between the foundation and the soil during changes in temperature, while the point where the displacement profile crosses the origin corresponds to the null point. In all cases, the slopes of the displacement profiles were observed to flatten with an increase in the change of temperature, reflecting greater displacements throughout the foundations with greater temperatures. However, the trends in the location of the null point observed in Figures 8(d) and 9(d) is inconsistent among the different tests, and is within the accuracy of the LVDT measurements of the head displacement. For the foundations in sand [Figure 8(d)], a slight downward movement was observed in the location of the null point for the foundations having a change in temperature of 7 and 12 °C, while a more significant upward movement was observed for the foundation with the largest change in temperature of 18 °C. For the foundations in silt [Figure 9(d)], a slight upward movement in the null point was observed for the test with a greater change in temperature. It is expected that the downward movement of the toe of the foundation during heating will mobilize end bearing resistance, leading to a stiffening response at the toe. Mimouni and Laloui (2014) evaluated energy foundations with a constant head stiffness, and found that the null point should move downward in response to an increase in restraint near the toe of the foundation with an increase in the change in temperature, albeit by a relatively small amount. The upward movement of the null point for the foundations in silt may possibly be associated with a stiffening of the soil near the head of the foundation due to greater thermally induced water flow in the soil in this region, which is a subject for further study. Overall, the trends in the data indicate that movement of the null point for semi-floating foundations may occur, but the magnitude of movement is expected to be minor. .

Effect of Soil Type on the Ultimate Capacity of Semi-Floating Foundations

The load settlement curves measured for Tests 1-4 and 5-7 are shown in Figures 10(a) and 10(b) for the semi-floating foundations in sand and silt, respectively. These curves were defined by zeroing the axial displacement and axial load at the beginning of mechanical loading. The foundations in all of the tests nearly reached a settlement corresponding to Davisson's criterion (Davisson 1973) before reaching the capacity of the pneumatic piston. The load-settlement curves for sand shown in Figure 10(a) are similar for all four average foundation temperatures, indicating a negligible effect of temperature on the load-settlement curve. However, the load-settlement curves for silt in Figure 10(b) show a similar increase in ultimate capacity with increasing temperature as that observed by McCartney and Rosenberg (2011). The difference in load-settlement behavior for the semi-floating foundations in sand and silt could be due to the comparatively low radial resistance provided by the sand compared to the compacted silt. The lateral stresses in the silt layer are initially much higher due to the compaction process than in the pluviated sand layer. Although Olgun et al. (2014) indicates that the amount of differential radial expansion of the foundation may not lead to significant changes in radial stress, the lateral stresses induced by compaction may have been sufficient to lead to a change in radial stress. Another possibility is that thermally-induced water flow may have affected the load-settlement curve of the foundations in Bonny silt as observed by Stewart and McCartney (2014). Although the two foundations tested at elevated temperatures were heated for similar durations before loading to failure, the greater temperature may have led to more drying of the soil around the foundation. This would lead to an increase in effective stress at the interface. This possibility reflects the importance of performing coupled flow-deformation modeling when energy foundations are used in unsaturated soils (Wang et al. 2014).

Effect of Head Restraint on Soil-Structure Interaction in End-Bearing Foundations

Profiles of different variables relevant to the evaluation of soil-structure interaction mechanisms in the end-bearing foundations in sand and silt layers are shown in Figures 11 and 12, respectively. The results in Figures 11(a) and 12(a) show the temperature distribution in the end-bearing foundations in sand and silt, respectively, for different average changes in temperature of the foundations. The profiles in Figure 11(a) correspond to the conditions near the end of heating, while those in Figure 12(a) correspond to the equilibrium conditions before (open symbols) and after (closed symbols) mechanical loading at each of the heating stages. The top and bottom of the foundations were slightly cooler than the center of the foundations, but the temperatures were relatively constant with depth within the foundations.

For these same instances in time, the thermal axial strains in the foundations are shown in Figures 11(b) and 12(b) for the end-bearing foundations in sand and silt, respectively. The thermal axial strains at a depth of zero for the foundation tested under load-control conditions in Figure 11(b) were not measured by the strain gages, but instead correspond to the theoretical thermal axial strain corresponding to free-expansion conditions. The strain at the foundation head is not known for the foundation tested under stiffness control conditions. Similar to the semi-floating foundation, the strains in the foundations in both soil layers are relatively close to the free expansion conditions. This is in contrast to the results presented by Stewart and McCartney (2014), possibly due to the much higher coefficient of thermal expansion of the reinforced concrete evaluated in this study. The thermal axial strain profiles in Figures 11(b) and 12(b) indicate that there is likely a slight bending strain induced in the end-bearing foundations due to off-axis loading. Although purely axial loading is difficult to control in the centrifuge for a precast concrete foundation, the effects of temperature can still be observed as a shift to smaller (more negative) thermal axial strains with heating. The points in these profiles are connected together with lines to better identify each data set, but in reality they encompass an envelope of strains on either side of the foundation.

The profiles of thermal axial stress are shown in Figures 11(c) and 12(c) for the foundations in sand and silt, respectively. In both soils, the thermal axial stress profiles are not as simple to interpret as those in the semi-floating foundation. Stewart and McCartney (2014) observed the greatest thermal axial stress at the bottom of the energy foundation. However, the shape of the profiles of thermal axial stress in the end-bearing foundations tested in this study is affected by the lower temperatures at the head and toe of the foundations, and cannot be directly compared with the hypothetical curves of Amatya et al. (2014) who assumed a constant temperature with depth. Nonetheless, this feature can be accounted for in simulations by using the temperature boundary conditions in the model (Goode 2013). The results in Figure 11(c) indicate that the foundation heated in stiffness-control conditions has greater stresses near the foundation head than the foundation heated in load-control conditions. Although more significant bending is observed in the results in Figure 12(c), the average trend in the data can be observed as the gages are on opposing sides of the foundation. The axial stress clearly increases during application of the mechanical load during each of the temperature stages. Similar to the semi-floating foundation tests, the magnitude of thermal axial stresses were greater in the silt layer than in the sand layers due to greater soil-structure interaction associated with higher initial radial stresses.

The profiles of thermal axial displacements shown in Figures 11(d) and 12(d) for the end-bearing foundations in sand and silt, respectively, were obtained by integrating the thermal axial strains with depth and assuming that the displacement at the bottom of the foundation is zero. Although this assumption implies that the null point is at the base of the foundation, this may not be the case for energy foundations bearing on more deformable geomaterials. The head displacement measured using the LVDTs at the surface are shown for verification purposes in Figure 11(d), and these values correspond very well with those obtained from the thermal axial strains. The results in Figure 12(d) indicate that the thermal axial displacements in the end-bearing foundation in silt decreased during mechanical loading of the foundation as expected.

Effect of Heating on the Load-Settlement Behavior of End-Bearing Foundations

The head displacement versus temperature of the end-bearing foundations in sand are shown in Figure 13(a), along with the change in axial load as a function of temperature. As expected, the load does not change with temperature for the load-control test, but the load increases with temperature corresponding to a stiffness of 113 kN/m in the stiffness-control test. The end-bearing foundation in the stiffness-control test shows slightly less head displacement than the foundation in the displacement-control test, although the difference is not significant. Nonetheless, this small difference in head displacement corresponded to an increase in axial stress at the head of the foundation of 100% as shown in Figure 11(c). More research using load-transfer analyses such as that of Knellwolf et al. (2011) are required to identify the range of head stiffness values encountered in the field to evaluate the full implications of head restraint.

The load-settlement curves for the end-bearing foundation in silt are shown in Figure 13(b). As mentioned in the discussion of the LVDT data in Figure 7(a), the initial loading stage led to a large, irrecoverable settlement. However, during each subsequent heating stage the slopes of the load-settlement curves were relatively consistent after each loading-unloading cycle. This either indicates that the temperature change does not have a significant impact on the side-shear stress distribution, which may have an impact on the slope of the load-settlement curve, or that the side shear stress was fully mobilized during the first loading cycle. The curves are also observed to shift upward with each temperature stage due to the effects of thermal expansion.

CONCLUSIONS

The impact of end restraint boundary conditions on the distributions in thermal axial stress and thermal axial displacement were evaluated using the results from a series of physical modeling experiments on centrifuge-scale energy foundations in dry sand and unsaturated silt layers. Specifically, the effects of end-bearing and semi-floating boundary conditions at the foundation toe and free-expansion and restrained-expansion boundary conditions at the foundation head were considered. The following specific conclusions can be drawn from the results:

- The thermal axial stresses were greater for energy foundations in compacted silt than in dry sand. This was attributed to greater soil-structure interaction due to the greater initial radial stresses in the compacted silt.
- The thermal axial stresses were greater for end-bearing energy foundations than semi-floating foundations due to the restraint provided by the rigid bottom boundary condition.
- An increase in thermal axial stress of nearly 100% was observed in the case where the head of an end-bearing foundation in dry sand was restrained than when it was permitted to expand upward freely.
- The results from the semi-floating foundations provide new insight into the potential behavior of energy foundations that obtain their axial capacity primarily through skin friction. The slope of the displacement curves were observed to consistently flatten with increasing temperature. Although a downward movement in the null point associated with increased restraint was expected with increasing temperature, inconsistent trends were observed in the data. An upward shift in the null point was observed in the foundations in silt potentially due to greater thermally-induced drying of the unsaturated silt around the head of

the foundation. Overall, the results indicate that only slight movements in the null point for semi-floating energy foundations are expected.

- Heating of semi-floating energy foundations in compacted silt was observed to lead to a clear increase in the ultimate capacity, but it led to a negligible effect for semi-floating energy foundations in sand. This was proposed to be due to a combination of radial stress changes and thermally-induced water flow in the unsaturated soil. The initial lateral stresses in the silt and sand differed due to different the preparation techniques, and a greater amount of differential radial thermal expansion may have occurred for the foundation in the silt due to the higher lateral stresses induced by compaction. Thermally-induced water flow away from the foundation is only expected in unsaturated soils, but will lead to an increase in effective stress on the soil-foundation interface. These effects are complex, and deserve simulation using coupled flow-deformation models that consider differential expansion of the foundation and soil.

ACKNOWLEDGMENTS

The authors would like to thank Dr. Min Zhang for her assistance in the centrifuge testing. Financial support from NSF grant CMMI-0928159 is gratefully acknowledged. The contents of this paper reflect the views of the authors and do not necessarily reflect the views of the sponsor.

APPENDIX I. REFERENCES

Amatya, B.L., Soga, K., Bourne-Webb, P.J., Amis, T., and Laloui, L. (2012). "Thermo-mechanical behaviour of energy piles." Géotechnique. 62(6), 503–519.

Akrouch, G., Sanchez, M., Briaud, J.-L. (2014). "Thermo-mechanical behavior of energy piles in high plasticity clays." Acta Geotechnica. 9(3), 399-412.

Bouazza, A., Singh, R.M., Wang, B., Barry-Macaulay, D., Haberfield, C., Chapman, G., Baycan, S., and Carden, Y. (2011). "Harnessing on site renewable energy through pile foundations." Australian Geomechanics. 46(4), 79-90.

Bourne-Webb, P.J., Amatya, B., Soga, K., Amis, T., Davidson, C. and Payne, P. (2009). "Energy pile test at Lambeth College, London: Geotechnical and thermodynamic aspects of pile response to heat cycles." Géotechnique. 59(3), 237–248.

Brandl, H. (1998). "Energy piles and diaphragm walls for heat transfer from and into the ground." Proceedings of the 3rd International Geotechnical Seminar on Deep Foundations on Bored and Auger Piles, BAP III, Ghent, Belgium. October 19-21. Balkema, Rotterdam. 37–60.

Brandl, H. (2006). "Energy foundations and other thermo-active ground structures." Géotechnique. 56(2), 81-122.

Davisson, M.T. (1973). "High capacity piles." "Innovation in Foundations Construction." Soil Mech. Div., Illinois Section, ASCE, Chicago, Ill., pp. 81-112.

Goode, J.C., III. (2013). Centrifuge Modeling of the Thermo-Mechanical Response of Energy Foundations. MS Thesis. University of Colorado Boulder. 221 pg.

Goode, J.C., III, Zhang, M. and McCartney, J.S. (2014). "Centrifuge modeling of energy foundations in sand." Proc. 8th International Conference on Physical Modelling in

Geotechnics (ICPMG 2014). Perth, Australia. January 14-17, 2014. CRC Press. pg. 729-736.

Goode, J.C., III and McCartney, J.S. (2014). "Evaluation of head restraint effects on energy foundations." Proceedings of GeoCongress 2014 (GSP 234), M. Abu-Farsakh and L. Hoyos, eds. ASCE. 2685-2694.

Knellwolf, C., Peron, H., and Laloui, L. (2011). "Geotechnical analysis of heat exchanger piles." ASCE Journal of Geotechnical and Geoenvironmental Engineering. 137(12), 890-902.

Laloui, L., Moreni, M. and Vulliet, L. (2003). "Comportement d'un pieu bi-fonction, foundation et échangeur de chaleur." Canadian Geotechnical Journal. 40(2), 388-402.

Laloui, L., Nuth, M. and Vulliet, L. (2006). "Experimental and numerical investigations of the behaviour of a heat exchanger pile." International Journal of Numerical and Analytical Methods in Geomechanics. 30(8), 763–781.

McCartney, J.S. and Rosenberg, J.E. (2011). "Impact of heat exchange on side shear in thermo-active foundations." Proc. Geo-Frontiers 2011 (GSP 211). J. Han and D.E. Alzamora, eds. ASCE, Reston VA. pg. 488-498.

McCartney, J.S. and Murphy, K.D. (2012). "Strain distributions in full-scale energy foundations." DFI Journal. 6(2), 28-36.

Mimouni T. and Laloui L. (2014). "Towards a secure basis for the design of geothermal piles." Acta Geotechnica. 9(3), 355-366. DOI 10.1007/s11440-013-0245-4.

Murphy, K.D., McCartney, J.S., Henry, K.H. (2014). "Thermo-mechanical response tests on energy foundations with different heat exchanger configurations." Acta Geotechnica. 1-17. DOI: 10.1007/s11440-013-0298-4.

Murphy, K.D. and McCartney, J.S. (2014). “Seasonal response of energy foundations during building operation.” Geotechnical and Geological Engineering. 1-14. DOI: 10.1007/s10706-014-9802-3.

Olgun, C.G., Ozudogru, T., and Arson, C.F. (2014). “Thermo-mechanical radial expansion of heat exchanger piles and possible effects on contact pressures at pile–soil interface.” Géotechnique Letters. 4(3) 170-178.

Ouyang Y., Soga K. and Leung Y.F. (2011). “Numerical back-analysis of energy pile test at Lambeth College, London.” Proc. Geo-Frontiers 2011 (GSP 211). J. Han and D.E. Alzamora, eds. ASCE, Reston VA. pg. 440-449.

Suryatriyastuti, M.E., Mroueh, H., and Burlon, S. (2013). “Chapter 7: Numerical analysis of the bearing capacity of thermoactive piles under cyclic axial loading.” Energy Geostructures. L. Laloui and A. DiDonna, eds. John Wiley and Sons. London.

Stewart, M.A. and McCartney, J.S. (2014). “Centrifuge modeling of soil-structure interaction in energy foundations.” ASCE Journal of Geotechnical and Geoenvironmental Engineering. 140(4), 04013044-1-11. DOI: 10.1061/(ASCE)GT.1943-5606.0001061.

Sutman, M., Brettmann, T., and Olgun, C.G., 2014. Thermo-mechanical behavior of energy piles: Full-scale field test verification. DFI 39th Annual Conference on Deep Foundations, Atlanta, GA. Oct. 21-24. pg. 1-11. (CD-ROM).

Wang, W., Regueiro, R., Stewart, M.A., and McCartney, J.S. (2012). “Coupled thermo-poro-mechanical finite element analysis of a heated single pile centrifuge experiment in saturated silt.” Proc., GeoCongress 2012 (GSP 225), R. D. Hryciw, A. Athanasopoulos-Zekkos, and N. Yesiller, eds., ASCE, Reston, VA. pg. 4406-4415.

Wang, B., Bouazza, A., Singh, R., Haberfield, C., Barry-Macaulay, D., and Baycan, S. (2014a). "Post-temperature effects on shaft capacity of a full-scale geothermal energy pile." J. Geotech. Geoenviron. Eng., 10.1061/(ASCE)GT.1943-5606.0001266, 04014125.

Wang, W., Regueiro, R. and McCartney, J.S. (2014b). "Coupled Axisymmetric Thermo-Poro-Elasto-Plastic Finite Element Analysis of Energy Foundation Centrifuge Experiments in Partially Saturated Silt." Geotechnical and Geological Engineering. 1-16. DOI: 10.1007/s10706-014-9801-4.

LIST OF TABLE AND FIGURE CAPTIONS

Table 1: Properties of Nevada sand and Bonny Silt used in the different experiments

Table 2: Details of centrifuge tests on semi-floating (short) and end-bearing (long) foundations

Fig. 1. Schematics of the scale model energy foundations including locations of the embedded strain gages and thermocouples

Fig. 2. Typical strain gage calibration results: (a) Individual gage correction before embedment; (b) Axial strain measurements in the long foundation after mechanical correction; (c) Thermal axial strain measurements in the long foundation after thermal correction

Fig. 3. Locations of instrumentation in the energy foundation tests

Fig. 4. Results from tests on semi-floating foundations in Nevada sand: (a, b, c, d) Load and displacement in Tests 1, 2, 3, 4; (e, f, g, h) Foundation temperatures in Tests 1, 2, 3, 4; (i, j, k, l) Axial strains in Tests 1, 2, 3, 4

Fig. 5. Results from tests on semi-floating foundations in Bonny silt: (a, b, c) Load and displacement for Tests 5, 6, 7; (d, e, f) Foundation temperatures for Tests 5, 6, 7; (g, h, i) Axial strains for Tests 5, 6, 7

Fig. 6. Results from tests on end-bearing foundations in Nevada sand: (a, b) Load and displacement in Tests 8 and 9; (c, d) Foundation temperatures in Tests 8 and 9; (e, f) Axial strains in Tests 8 and 9

Fig. 7. Results from a test on an end-bearing foundation in Bonny silt (Test 10): (a) Load and displacement; (b) Foundation temperatures; (c) Axial strains

Fig. 8. Synthesis of thermo-mechanical behavior of semi-floating foundations in Nevada sand (Tests 2-4): (a) Temperature profiles; (b) Thermal axial strain profiles; (c) Thermal axial stress profiles; (d) Thermal axial displacement profiles

Fig. 9. Synthesis of thermo-mechanical behavior of semi-floating foundations in Bonny silt (Tests 6 and 7): (a) Temperature profiles; (b) Thermal axial strain profiles; (c) Thermal axial stress profiles; (d) Thermal axial displacement profiles

Fig. 10. Summary of load-displacement curves for semi-floating energy foundations under different temperatures (a) Nevada sand (Tests 1-4); (b) Bonny silt (Test 5-7)

Fig. 11. Synthesis of thermo-mechanical behavior of end-bearing foundations in Nevada sand (Tests 8 and 9): (a) Temperature profiles; (b) Thermal axial strain profiles; (c) Thermal axial stress profiles; (d) Thermal axial displacement profiles

Fig. 12. Synthesis of thermo-mechanical behavior of an end-bearing foundation in Bonny silt in Test 10 (open symbols: before loading; closed symbols: after loading): (a) Temperature profiles; (b) Thermal axial strain profiles; (c) Thermal axial stress profiles; (d) Thermal axial displacement profiles

Fig. 13. Load-settlement behavior of end-bearing foundations in different soil layers: (a) Nevada Sand (Tests 8 and 9); (b) Bonny silt (Test 10)

Table 1: Properties of Nevada sand and Bonny silt used in the different experiments

Parameter	Nevada Sand	Bonny Silt
D_{10}	0.09 mm	< 0.0013 mm
D_{30}	0.11 mm	0.022 mm
D_{50}	0.16 mm	0.039 mm
% Passing No. 200 Sieve	0	83.9 %
% Clay Size	0	14.0 %
% Silt Size	0	69.9 %
% Sand Size	100	16.1 %
G_s	2.65	2.6
Liquid Limit, LL	-	25
Plastic Limit, PL	-	21
Plasticity Index, PI	-	4
Activity, A	-	0.29
Effective friction angle, ϕ	35°	32.4°
Compression index, C_c	-	0.015
Recompression index, C_r	-	0.0017
Std. Proctor Max. Dry Unit Weight	-	16.9 kN/m^3
Std. Proctor Max. Opt. Water Content	-	13.6%
Initial void ratio, e_0	0.75	0.63
Initial water content, w_0	0	14.2%
Initial degree of saturation, S_0	0	0.59
Saturated hydraulic conductivity, k_s	1.0×10^{-4} m/s	7.6×10^{-8} m/s
Thermal conductivity for e_0 and S_0, λ	0.25	1.147 W/mK

Table 2: Details of centrifuge tests on semi-floating (short) and end-bearing (long) foundations

(Note: All tests performed at a g-level of 24)

Test	Soil	Foundation	Load or Stiffness Control	Soil Total Unit Weight	Comp. Water Content	Thermal Conductivity	T_{ave} at Loading to Failure	ΔT_{ave} at Loading to Failure
				(kN/m^3)	(%)	W/(mK)	(^oC)	(^oC)
1	Nevada	Short	Load	15.5	-	-	23.0	0.0
2	Nevada	Short	Load	15.5	-	-	30.2	7.0
3	Nevada	Short	Load	15.5	-	0.265	35.3	12.0
4	Nevada	Short	Load	15.5	-	-	40.3	18.0
5	Bonny	Short	Load	17.0	12.3	1.234	21.4	0.0
6	Bonny	Short	Load	17.0	12.6	1.237	30.5	10.0
7	Bonny	Short	Load	17.0	12.5	1.252	38.0	18.0
8	Nevada	Long	Load	15.5	-	-	33.4	11.1
9	Nevada	Long	Stiffness	15.5	-	-	33.3	11.8
10	Bonny	Long	Load	17.0	12.2	1.150	21.6, 31.1, 36.3, 37.5, 27.7	0.0, 9.5, 14.7, 15.9, 6.1

1
Click here to download high resolution image

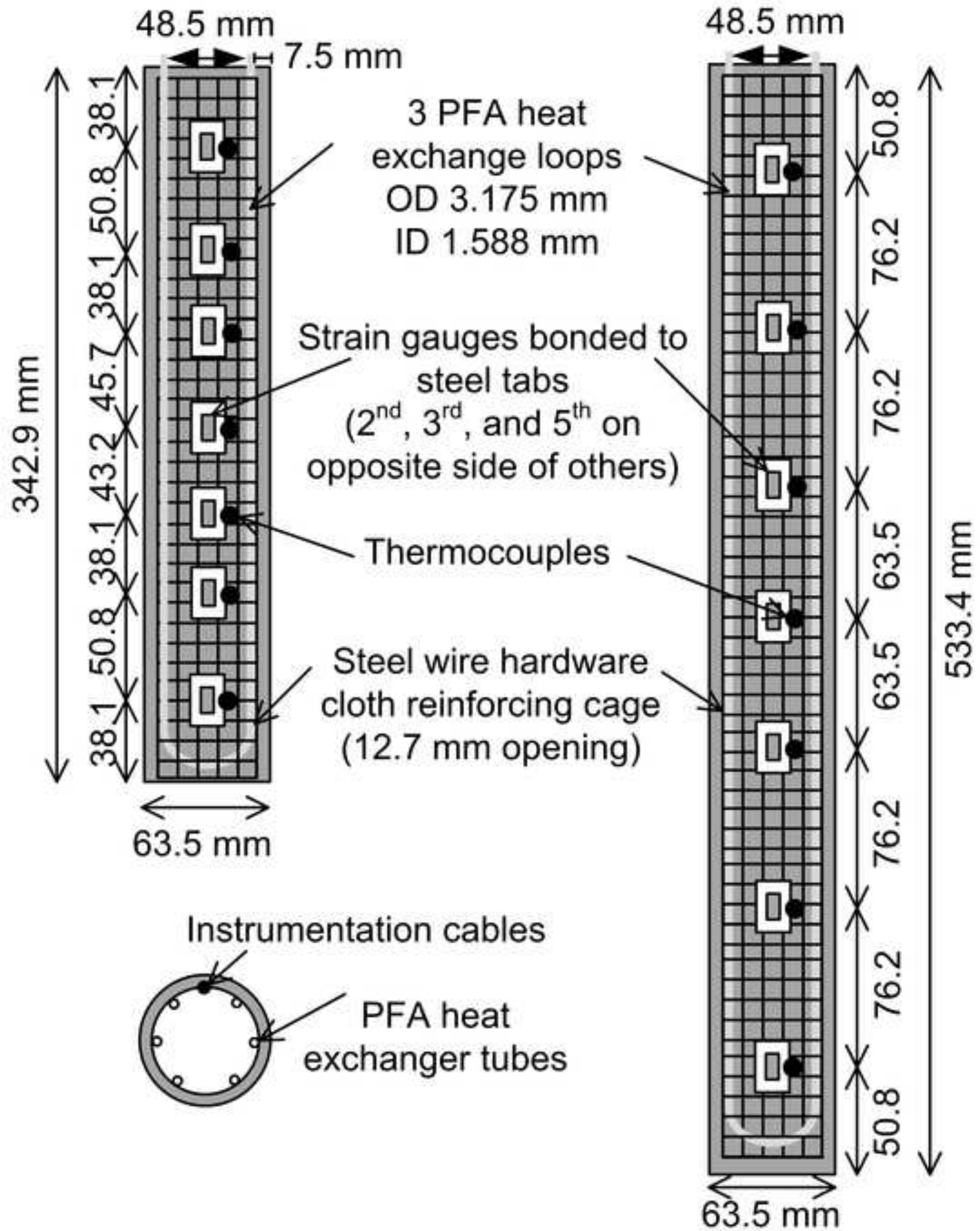

2
Click here to download high resolution image

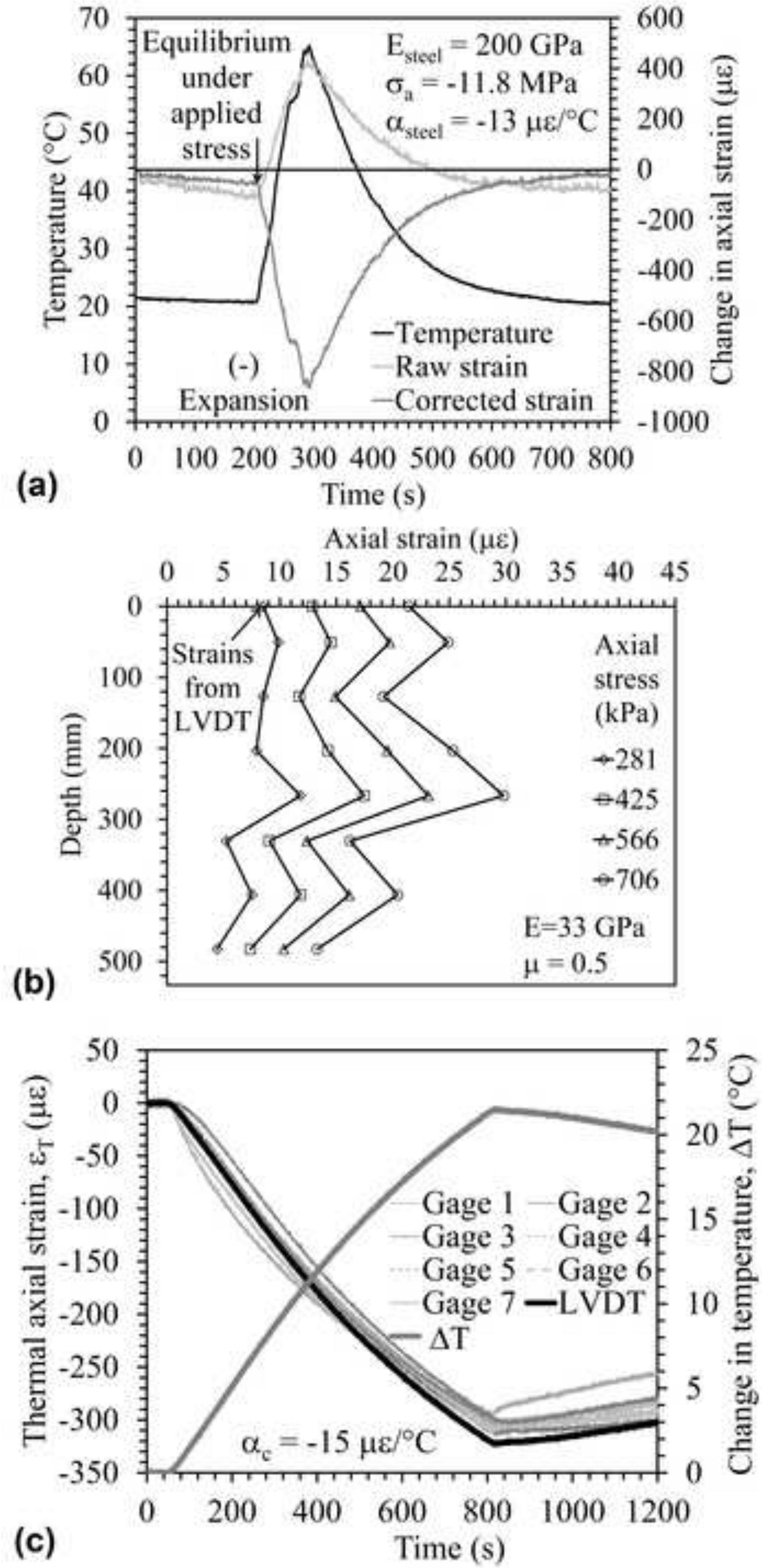

3
Click here to download high resolution image

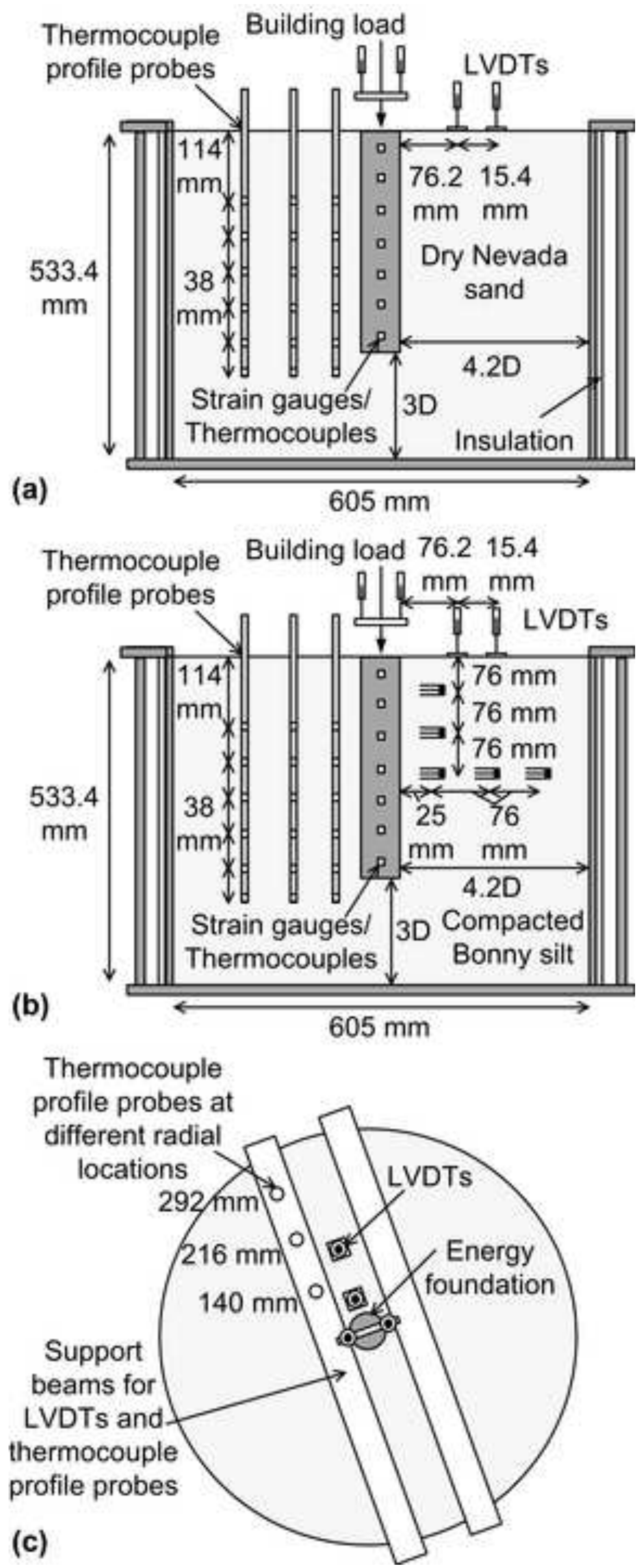

4

Click here to download high resolution image

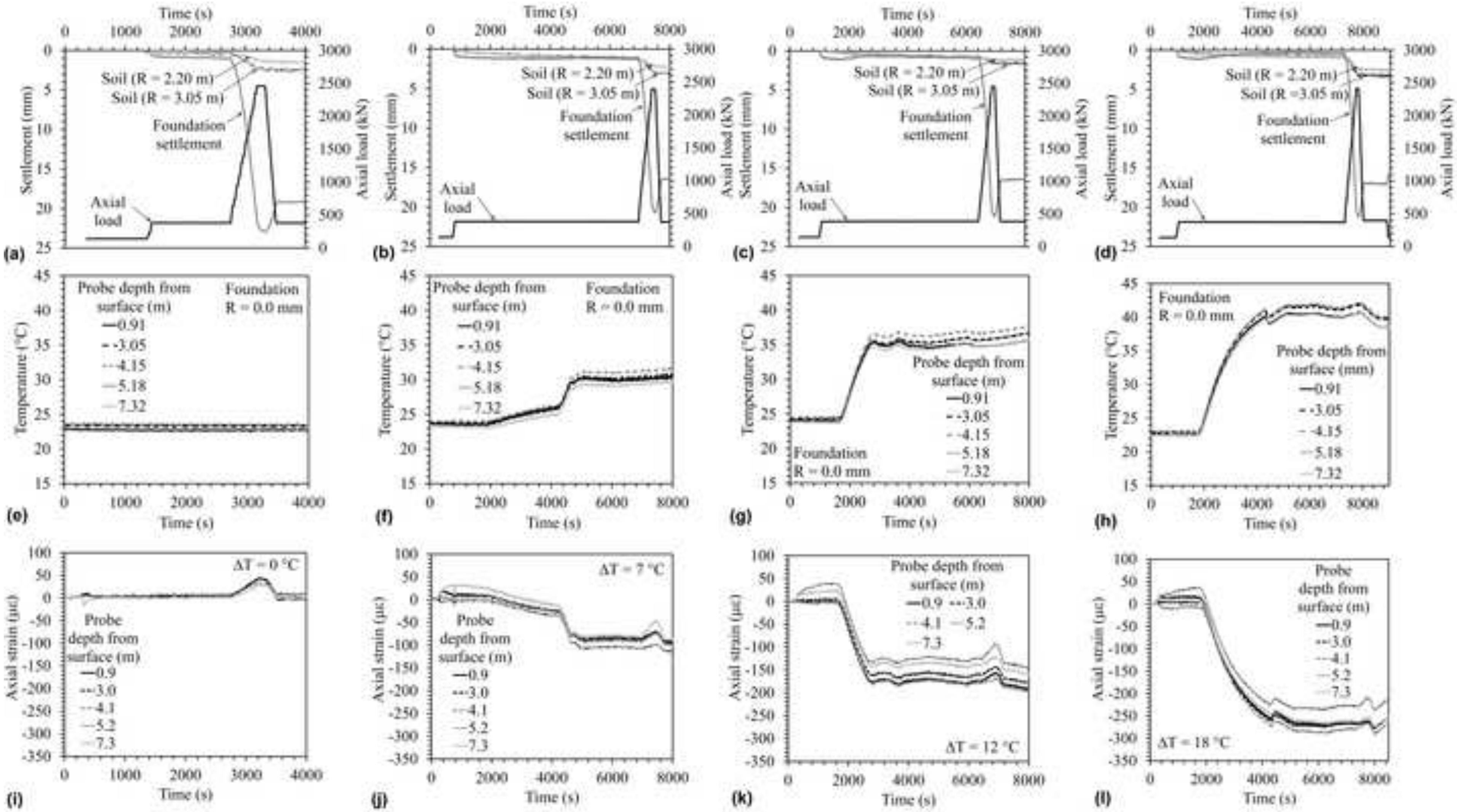

5

Click here to download high resolution image

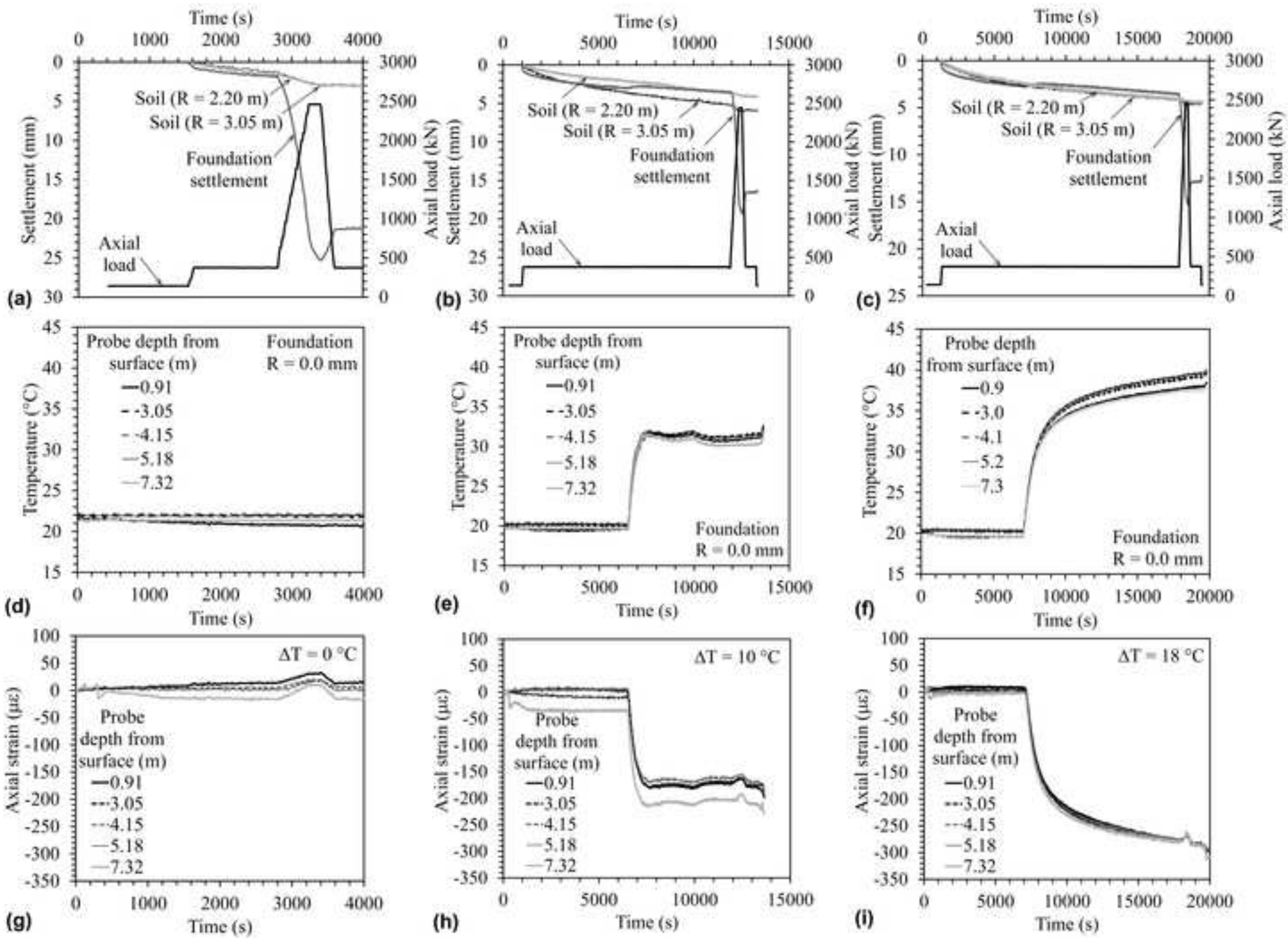

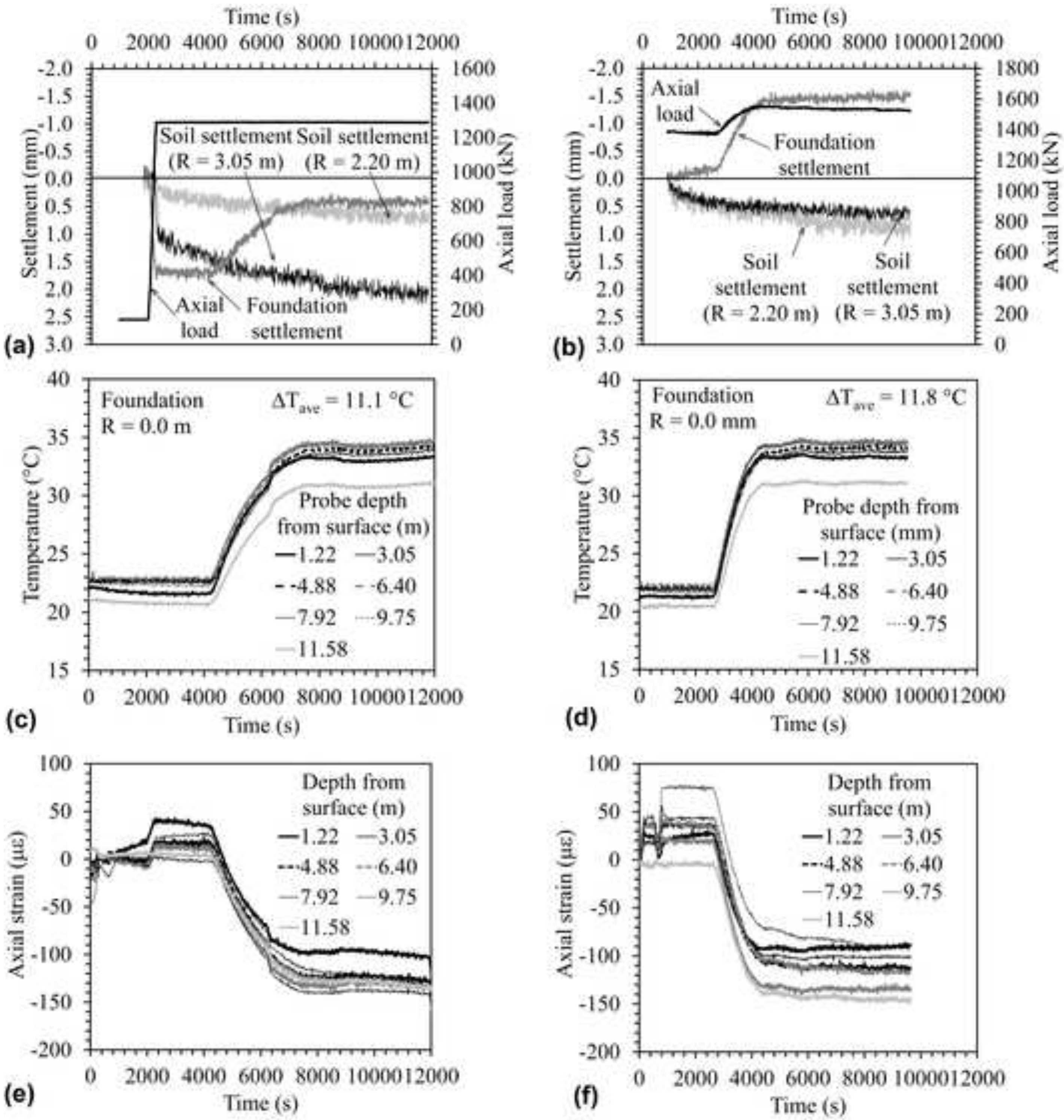

(a)
Time (s)
Settlement (mm)
Axial load (kN)
Soil settlement (R = 3.05 m)
Soil settlement (R = 2.20 m)
Axial load
Foundation settlement
(b)
Axial load
Foundation settlement
Soil settlement (R = 2.20 m)
Soil settlement (R = 3.05 m)
(c)
Foundation R = 0.0 m
ΔT_{ave} = 11.1 °C
Temperature (°C)
Probe depth from surface (m)
1.22
3.05
4.88
6.40
7.92
9.75
11.58
(d)
Foundation R = 0.0 mm
ΔT_{ave} = 11.8 °C
Probe depth from surface (mm)
(e)
Axial strain (με)
Depth from surface (m)
(f)

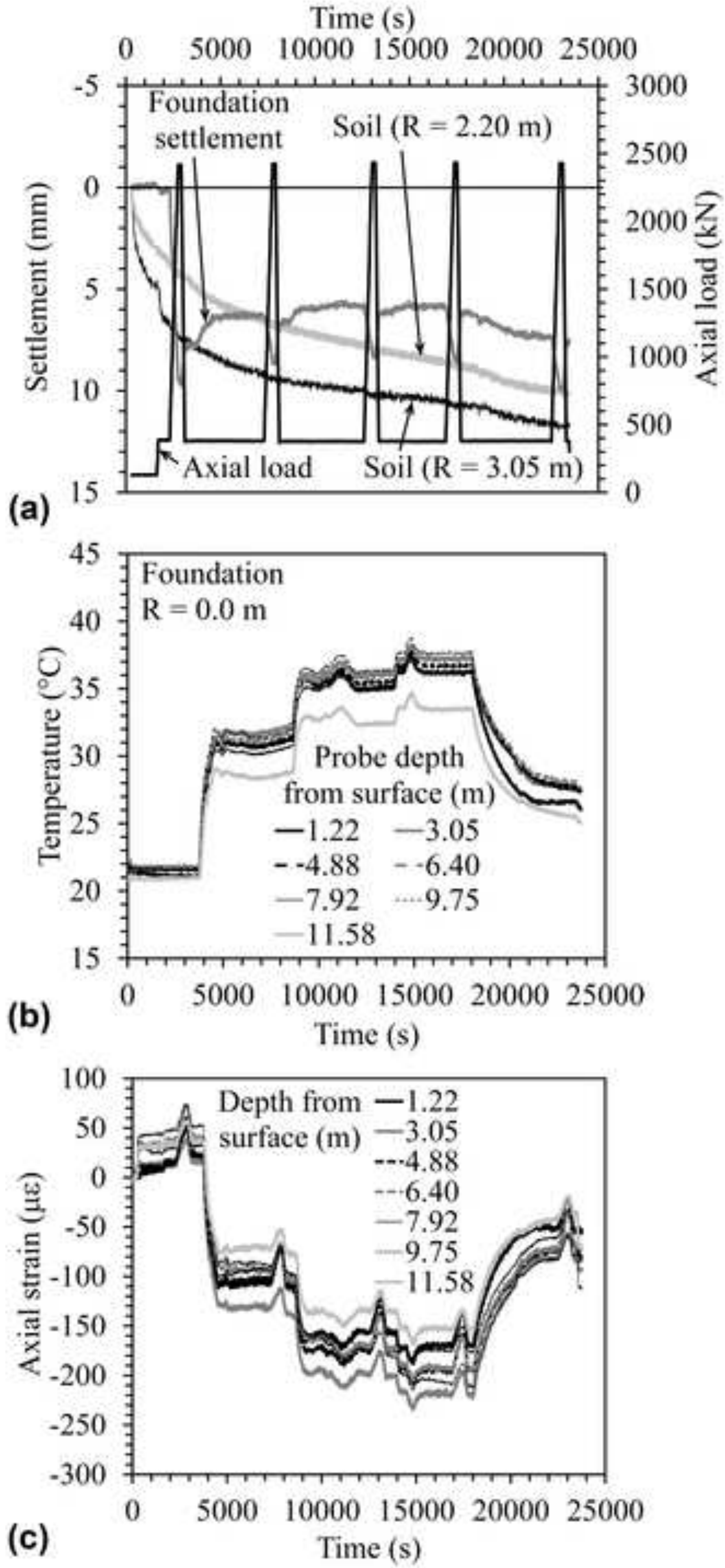
Time (s)
0 5000 10000 15000 20000 25000
Settlement (mm)
Axial load (kN)
Foundation settlement
Soil (R = 2.20 m)
Axial load
Soil (R = 3.05 m)
(a)
Temperature (°C)
Foundation
R = 0.0 m
Probe depth from surface (m)
1.22
3.05
4.88
6.40
7.92
9.75
11.58
(b)
Axial strain (με)
Depth from surface (m)
1.22
3.05
4.88
6.40
7.92
9.75
11.58
(c)

8

Click here to download high resolution image

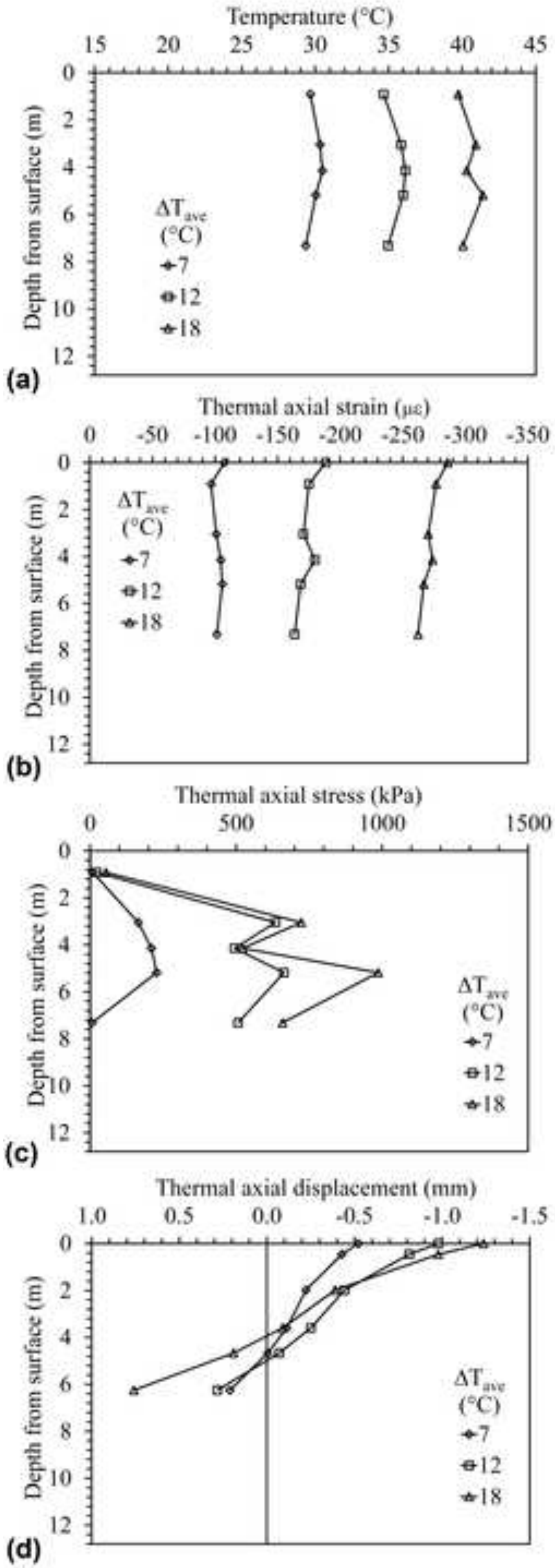

9

Click here to download high resolution image

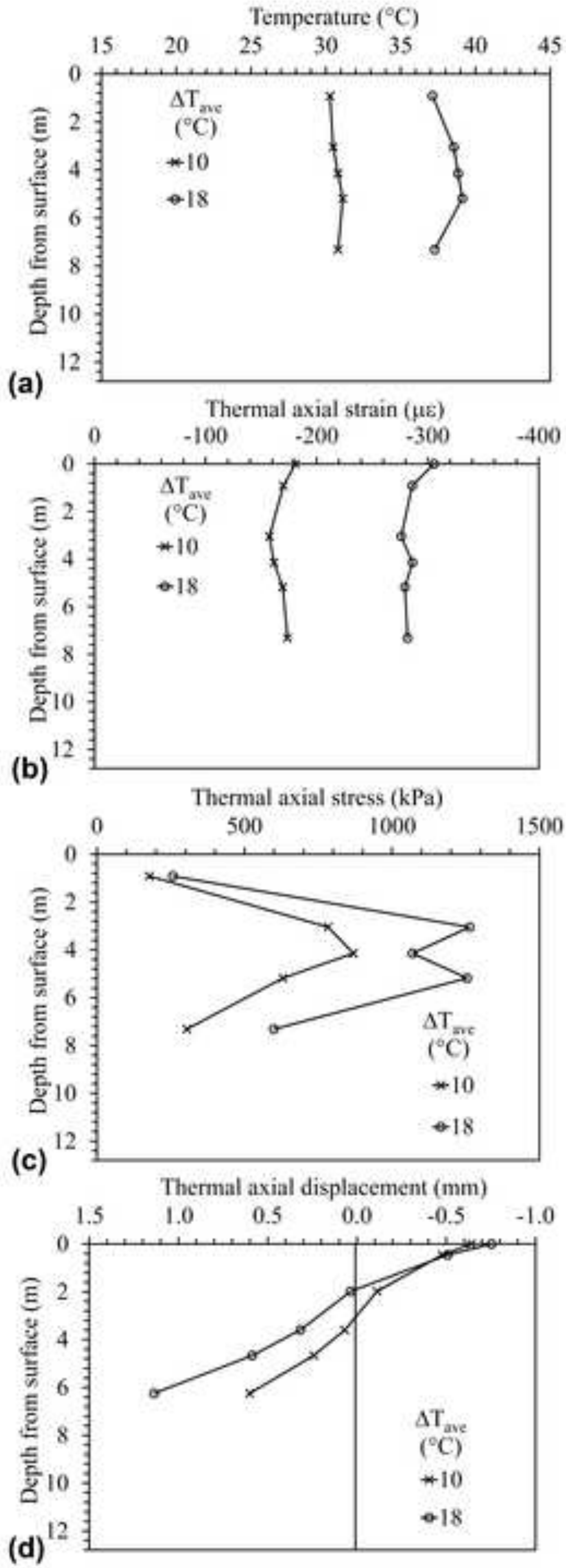

10
Click here to download high resolution image

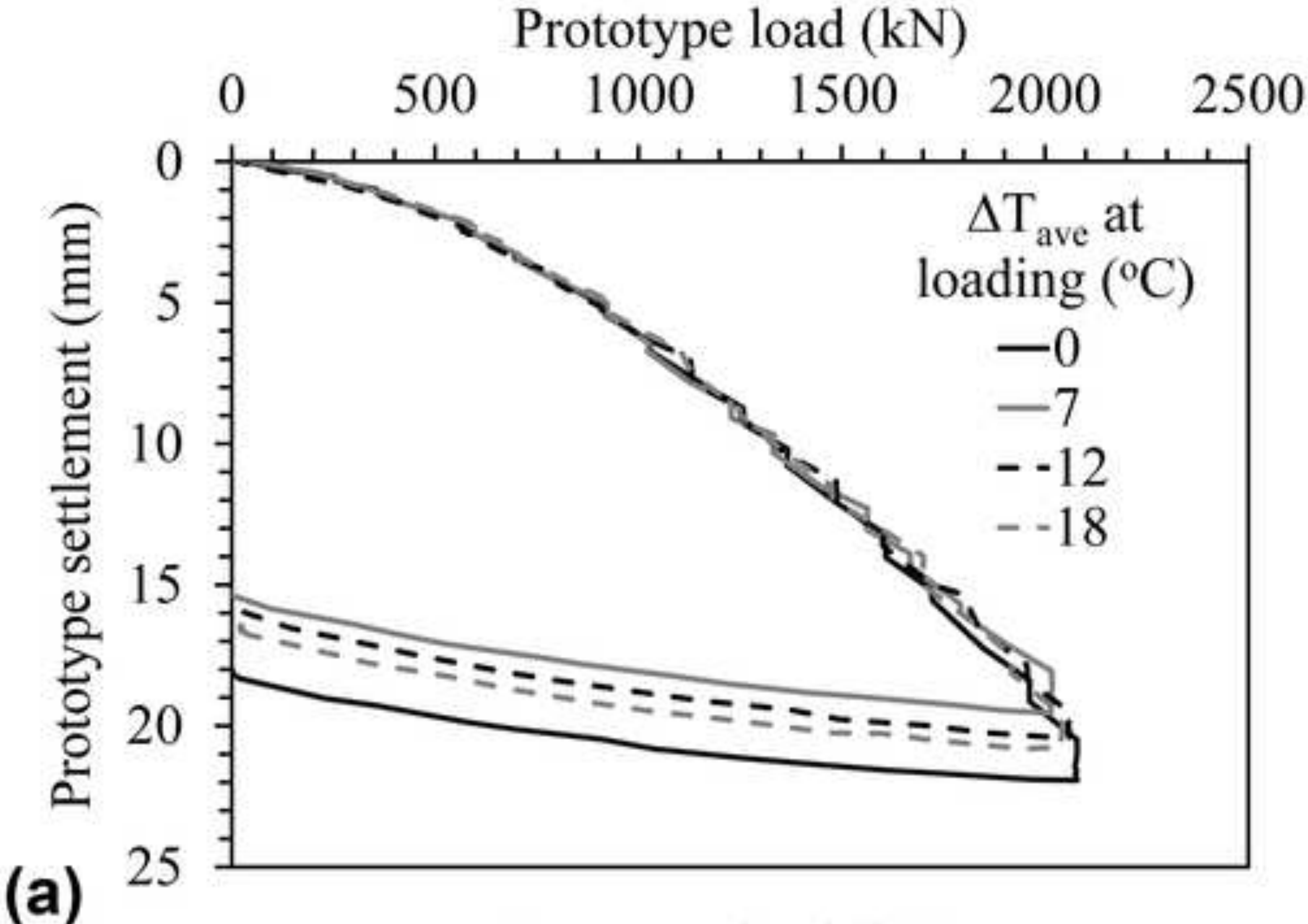

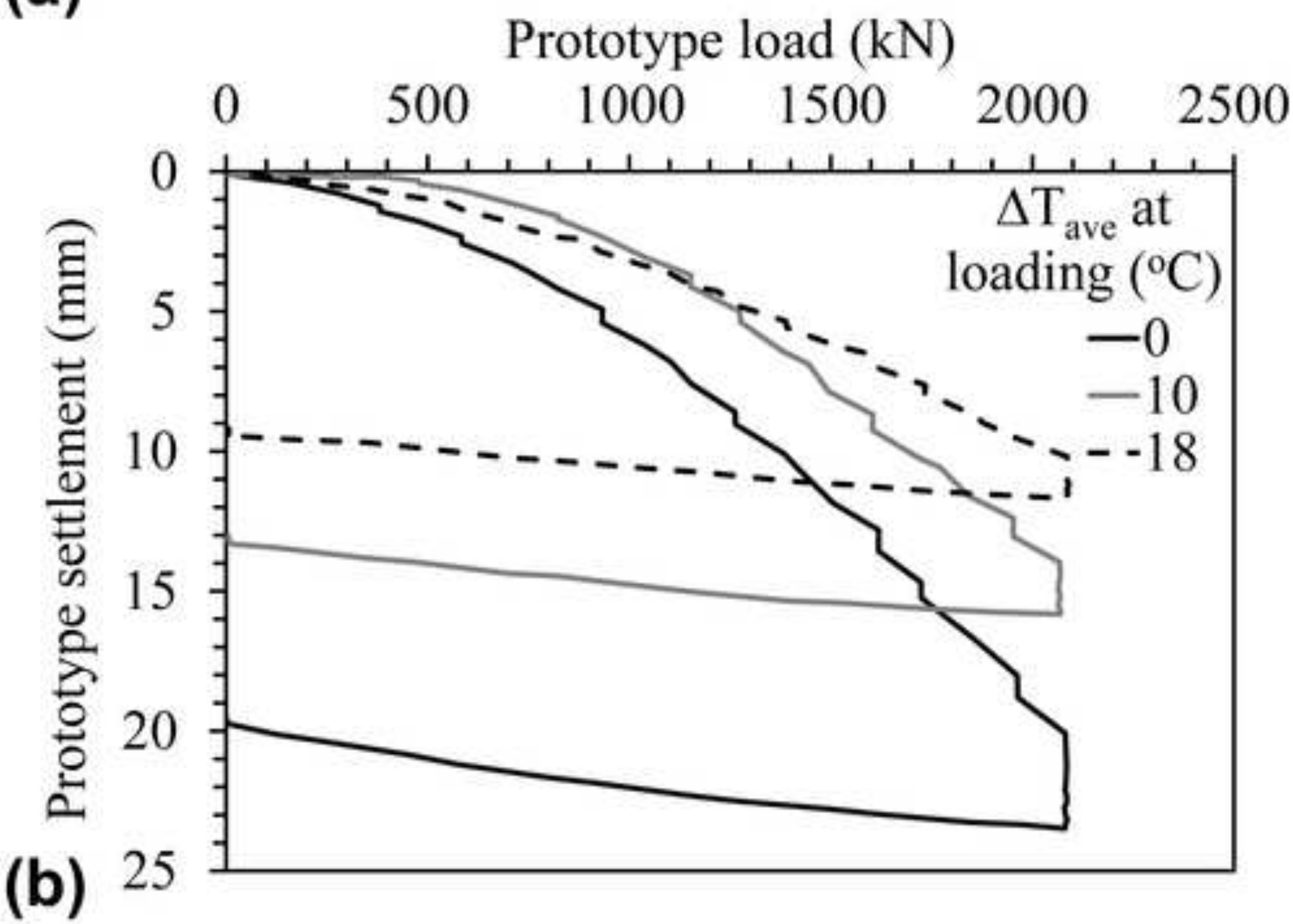

11
Click here to download high resolution image

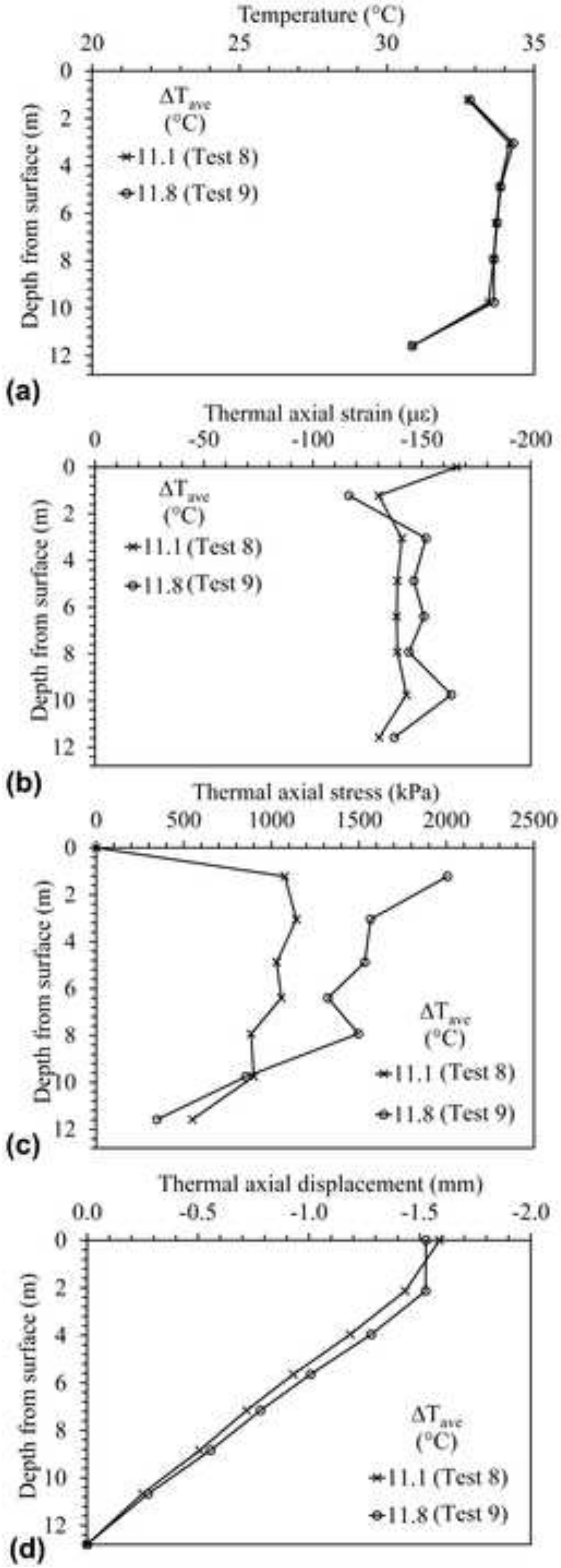

12

Click here to download high resolution image

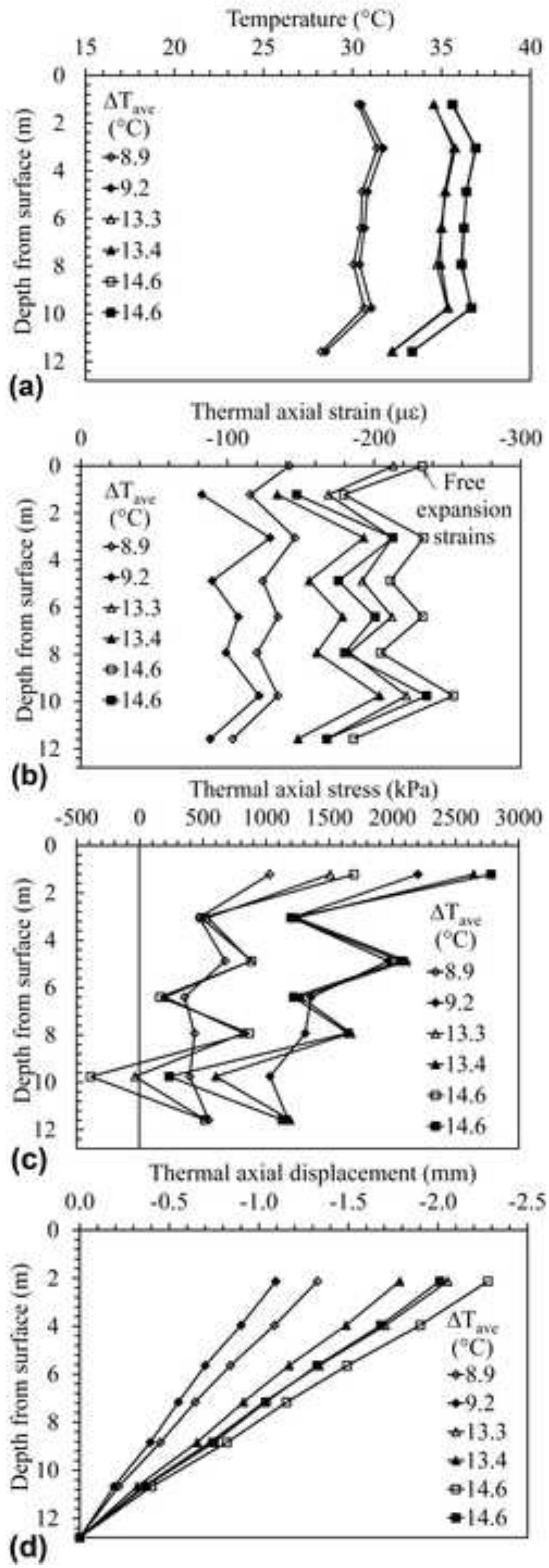

13
Click here to download high resolution image